Thermal Management of a 48V Lithium-Ion Battery Pack by Semiconductor Refrigeration

Rui Yang[1,2], Kuining Li[1,2*], Yi Xie[3], Wei Li[3], Yuping Qian[4], Yangjun Zhang[4] and Hongxiang Zhang[1,2]

[1]Key Laboratory of Low-grade Energy Utilization Technologies and Systems (Chongqing University), Ministry of Education of China, Chongqing University, Chongqing, China, [2]School of Energy and Power Engineering, Chongqing University, Chongqing, China, [3]College of Mechanical and Vehicle Engineering, Chongqing University, Chongqing, China, [4]State Key Lab of Automotive Safety and Energy, School of Vehicle and Mobility, Tsinghua University, Beijing, China

At present, 48 V mild hybrid battery systems are widely used in hybrid electric vehicles to reduce fuel consumption and emissions. The battery pack often operates at high discharge/charge rates and requires an efficient and compact battery thermal management system (BTMS) to control its temperature, improve its electrical performance and extend its life. Due to their short start-up times and simple structures, semiconductors can provide rapid refrigeration and cool a battery quickly in response to sudden high current rates. Therefore, semiconductors were applied to the BTMS of a 48 V battery. The performance of the semiconductor-based BTMS was studied by simulation and experiment at high discharge rates (up to 9.375 C). Firstly, a thermal model of the BTMS was developed that integrates a resistance-based battery thermal model, a semiconductor thermal model and a three-dimensional fluid-solid coupled heat transfer model. Unlike a traditional thermal model, the proposed model considers the joint influences of SOC, temperature and current on battery resistance and improves the predictive precision of the battery's thermal behaviour. The thermal model was verified by an experiment, with the results showing that it could precisely describe the temperature increase in the battery (maximum average absolute error within 0.9°C). Finally, the BTMS thermal model was applied to predict the cooling performance of the semiconductor BTMS at an ambient temperature of 37°C and high current rates (up to 9.375 C), which was compared with that of an air-cooled BTMS. The results demonstrate that the semiconductor-based BTMS achieves lower battery temperature than the air-cooled BTMS and ensures a temperature difference within the 48 V pack of <1.6°C.

Keywords: 48 V battery pack, battery thermal management system, semiconductor refrigeration, battery thermal behaviour, high ambient temperature, high discharge rate

1 INTRODUCTION

Over the past decade, new energy vehicles have rapidly become a technological focal point, as they can reduce fossil fuel consumption and the negative environmental impacts of vehicular traffic (including ground-level ozone, regional smog and climate change) (Dunn et al., 2011). Hybrid electric vehicles (HEVs) are a combination of fossil-fuelled and electric vehicles (EVs). They use an electric motor in parallel with an internal combustion engine (ICE) and also have a kinetic energy

recovery function, which saves energy and reduces fuel costs while ensuring range (Maggetto and Van Mierlo, 2001; Bradley and Quinn, 2010). Compared with regular hybrid technology, the 48 V mild hybrid system offers better space utilization and easier integration with ICE-based powertrains, as well as lighter weight and lower cost (Ran et al., 2017; Lee et al., 2018; Yu et al., 2018).

Lithium-ion batteries are used as the power source in 48 V systems because of their good energy density, power density and service life. However, high-power 48 V battery pack systems produce high amounts of heat, which directly affects battery performance, lifetime and safety (Yang et al., 2014; Placke et al., 2017; Huang et al., 2018). For optimal battery performance, its operating temperature needs to be controlled within 25–40°C, and the temperature difference between battery cells should not exceed 5°C (Pesaran, 2002; Malik et al., 2016; Al-Zareer et al., 2017). Therefore, a battery thermal management system (BTMS) is necessary to ensure performance and avoid accidents such as combustion and explosion caused by thermal runaway (Ianniciello et al., 2018).

Currently, BTMSs have achieved cooling using air, liquid, heat pipes, phase-change materials and semiconductor-based thermoelectric cooling (TEC). Semiconductor cooling has received widespread attention for its short start-up time, simple structure and ability to achieve rapid cooling under instantaneous high currents. It is usually combined with one or more other cooling methods. In 2003, Alaoui et al. (Alaoui and Salameh, 2003; Alaoui and Salameh, 2005) were the first to study BTMSs based on TEC technology for use in EVs and demonstrated their feasibility. Li, Song, and Lyu (Song et al., 2018; Li et al., 2019; Lyu et al., 2019) combined TEC with forced-air, phase-change material, and liquid cooling methods to improve the cooling of battery modules. Song, Sirikasemsuk, and Seo (Seo et al., 2018; Song et al., 2018; Sirikasemsuk et al., 2021) investigated the effects of TEC parameters such as semiconductor arrangement, optimal ambient temperature range, cooling power and voltage on cooling. Liu (Liu et al., 2014) further verified the effectiveness of TEC systems at high temperatures. In the above studies, the accurate prediction of cell temperatures and heat production is related to the design and validation of the BTMS. Therefore, the relationships between the electrical and thermal characteristics of Li-ion batteries need to be established (Kim et al., 2011). The battery energy balance system proposed by Bernardi (Bernardi et al., 1985) provides a theoretical basis for calculating battery heat production. Electrochemical-thermal and electro-thermal models were established, both of which can calculate external characteristics such as charge-discharge curves and temperature distributions. However, the estimates of some internal characteristics may differ when different models are used. Electrochemical-thermal models analyse the influence of electrochemical parameters on thermal properties. They describe electrode reaction kinetics using the Butler-Volmer equation and the diffusion of particles in the electrolyte or active material by Fick's law. These models focus on the parameters and properties of the cell materials, such as particle size and solid-liquid diffusion coefficient, and require a large number of electrochemical parameters (Tang et al., 2019). In contrast, electro-thermal models use empirical equations to describe the potential and current density distribution on the electrode, so focus on the electrical properties of the cell (such as open-circuit voltage and entropy coefficient). Their advantages of requiring fewer parameters and less calculation make them more suitable for studying the effects of macroscopic parameters on cell performance, such as cell size and internal resistance. In HEVs, 48 V battery systems require an instantaneous discharge rate close to 10 C to satisfy the power requirements. At high ambient temperatures, such high currents are a great challenge in terms of battery heat dissipation. Therefore, the performance of the TEC systems used in BTMSs needs to be studied under high currents and temperatures.

To overcome the shortcomings of present semiconductor-based BTMS (SBTMS) studies, this paper develops three models to study the performance of 48 V battery packs with coupled TEC–forced-air cooling at high discharge rates and temperatures: 1) a resistance-based battery thermal model, 2) a semiconductor thermal model and 3) a three-dimensional fluid-solid coupled heat transfer model. The contributions of this paper are 1) the development of a battery model and 2) validation of the effect of TEC at high currents and ambient temperatures. The first contribution involves the development of a resistance-based battery body thermal model that considers the dependence of ohmic resistance and polarization resistance on battery SOC (tested range = 0.1–1), current (at 3.125, 6.25, 9.375 and 12.5 C) and ambient temperature (tested range = 5–40°C). A thermal model of battery tabs is also established due to the drastic effect of the tabs' ohmic heat on the cells' temperature distribution. A complete battery thermal model is developed to accurately predict the heat production and temperature distribution of the battery. The second contribution involves testing the performance of TEC by simulation of a 48 V battery system at a discharge rate of 9.375 C and ambient temperature of 37°C.

In this paper, an eight A h LiFePO$_4$ pouch battery and 72,001/241/060B semiconductor are used as the research objects. Thermal models of the battery and semiconductor are established and verified through experiments. Then, a 48 V battery pack BTMS coupled with TEC and forced-air cooling is built to test cooling performance at an ambient temperature of 37°C and high current rates of up to 9.375 C.

2 POUCH BATTERY CELL THERMAL MODEL

Assuming that the thermal conductivity of the cell is anisotropic, the rest of each material physical parameters are isotropic and do not vary with the temperature. By Fourier's law, the three-dimensional unsteady heat transfer model of the lithium battery cell can be expressed as (Yang and Tao, 2006):

$$\rho C_{\mathrm{P}}\frac{\partial T}{\partial t} = k_x\frac{\partial^2 T}{\partial x^2} + k_y\frac{\partial^2 T}{\partial y^2} + k_z\frac{\partial^2 T}{\partial z^2} + q \qquad (1)$$

where ρ is the battery density; C_{p} is its specific heat capacity; T is the battery temperature; t is time; k_x, k_y and k_z are the thermal conductivities of the battery in the x-, y- and

z-directions, respectively; and q is the heat generation rate of the battery.

2.1 Battery Cell Heat Generation Model
2.1.1 Battery Body

During charge/discharge processes, the cell has four heat sources according to Ref. (Bernardi et al., 1985): electrochemical reaction heat, ohmic heat, polarization heat and side reaction heat (always ignored). Newman (Thomas and Newman, 2003) linked the electrochemical parameters with the electrical and thermal parameters that can be easily measured to describe the heat sources. Because the difference between the cell terminal voltage and open-circuit voltage (OCV) can be expressed in terms of current and resistance, the heat production inside the cell can be calculated by:

$$Q_{\text{total}} = I(U - V) + IT\frac{dU}{dT} = I^2(R_o + R_P) + IT\frac{dU}{dT} \quad (2)$$

where Q_{total} is the total heat generation inside the cell, I is the current through the cell, V is the cell terminal voltage, U is the OCV, T is the cell temperature, dU/dT is the entropy coefficient, R_o is the ohmic resistance, R_p is the polarized resistance, $I^2 R_o$ is ohmic heat, $I^2 R_p$ is polarization heat, and $ITdU/dT$ is electrochemical reaction heat. The heat production per unit volume inside the cell q_{cell} is:

$$q_{\text{cell}} = \frac{Q_{\text{total}}}{V_{\text{b}}} = \frac{1}{V_{\text{b}}}\left(I^2(R_o + R_p) + IT\frac{dU}{dT}\right) \quad (3)$$

where V_{b} is the cell volume (m^3).

2.1.2 Tabs

Tabs are the metal conductors connecting the cells to the external charging and discharging equipment. They have a strong impact on the temperature distribution of a pouch battery. According to Ref. (Xie et al., 2020), the heat conducted between a tab and the battery body can be ignored at low-current discharge rates because there is little heat conduction. Thus, according to the first law of thermodynamics, the simplified energy balance inside a tab is:

$$I^2 R_{\text{tab},j} = m_{\text{tab},j}C_{\text{p,tab},j}\frac{dT_{\text{tab},j}}{dt} + h_{\text{tab},t}A_{\text{tab},t}\Delta T_{\text{tab},j}, \ (j = p, n) \quad (4)$$

where $R_{\text{tab},j}$ is the total resistance of the tab, which is the sum of the contact resistance R_c and tab resistance R_t, m_{tab} is the tab mass, $C_{\text{p,tab}}$ is specific heat capacity of the tab, T_{tab} is the tab temperature, h_{tab} is the heat transfer coefficient between the tab and the air, A_{tab} is the tab area, ΔT_{tab} is the difference between the tab and ambient temperatures, and subscript j represents tab's polarity (positive = p, negative = n). The heat generation rate inside the tab q_{tab} can be obtained by solving:

$$q_{\text{tab},j} = \frac{I^2 R_{\text{tab},j}}{V_{\text{tab},j}} \quad (5)$$

where $V_{\text{tab},j}$ is the tab volume, which is $1.152 \times 10^{-6} \ m^3$ in the studied pouch battery.

TABLE 1 | Main technical parameters of the lithium-ion battery and 48 V battery pack.

Parameter	Technical specification	
	Cell	Pack
Anode material	Graphite	Graphite
Cathode material	LiFePO$_4$	LiFePO$_4$
Electrolyte material	LiPF$_6$	LiPF$_6$
Size (mm)	4.8 × 160 × 227	304 × 96 × 180
Mass (kg)	0.33	5
Nominal capacity (A·h)	8	8
Nominal voltage (V)	3.3	48
Voltage range (V)	2.4–3.65	54–24
Operating temperature (°C)	−30–55	−30–55

2.2 Parameters of the Thermal Model
2.2.1 Battery Resistance and Entropy Coefficient

In this paper, an 8 Ah lithium-ion pouch battery produced by A123 was adopted to study the thermal performance of the SBTMS. **Table 1** shows its technical parameters. Hybrid pulse power characterization (HPPC) tests were implemented to obtain the cell resistance according to the process given in Ref. (Stroe et al., 2018). The cell OCV was measured before each impulse current in the HPPC and the entropy coefficient was calculated based on the OCVs at different battery temperatures. **Figure 1** shows the experimental devices: the current load on the cell was provided by a NEWARE CE-7001 PACK battery tester, a thermostat was used to control the desired ambient temperature of the cell, and the body temperature of the cell was monitored by K-type thermocouples attached to the cell surface. The layout of temperature measurement points on the cell is also shown in **Figure 1**. The cell temperature, voltage and current were recorded by computers. The relative error of the temperature sensor was ±0.75%.

Figure 2A–D show the variations in cell ohmic resistance and polarized resistance with SOC, cell temperature and current. A polynomial responding surface model (PRSM) was adopted to fit these data, and the results are:

$$R_o(I, SOC, T) = \sum_{i=1}^{4}A_i^{(1)}I^i + \sum_{i=1}^{4}B_i^{(1)}SOC^i + \sum_{i=1}^{4}C_i^{(1)}T^i + D^{(1)}I \cdot SOC$$
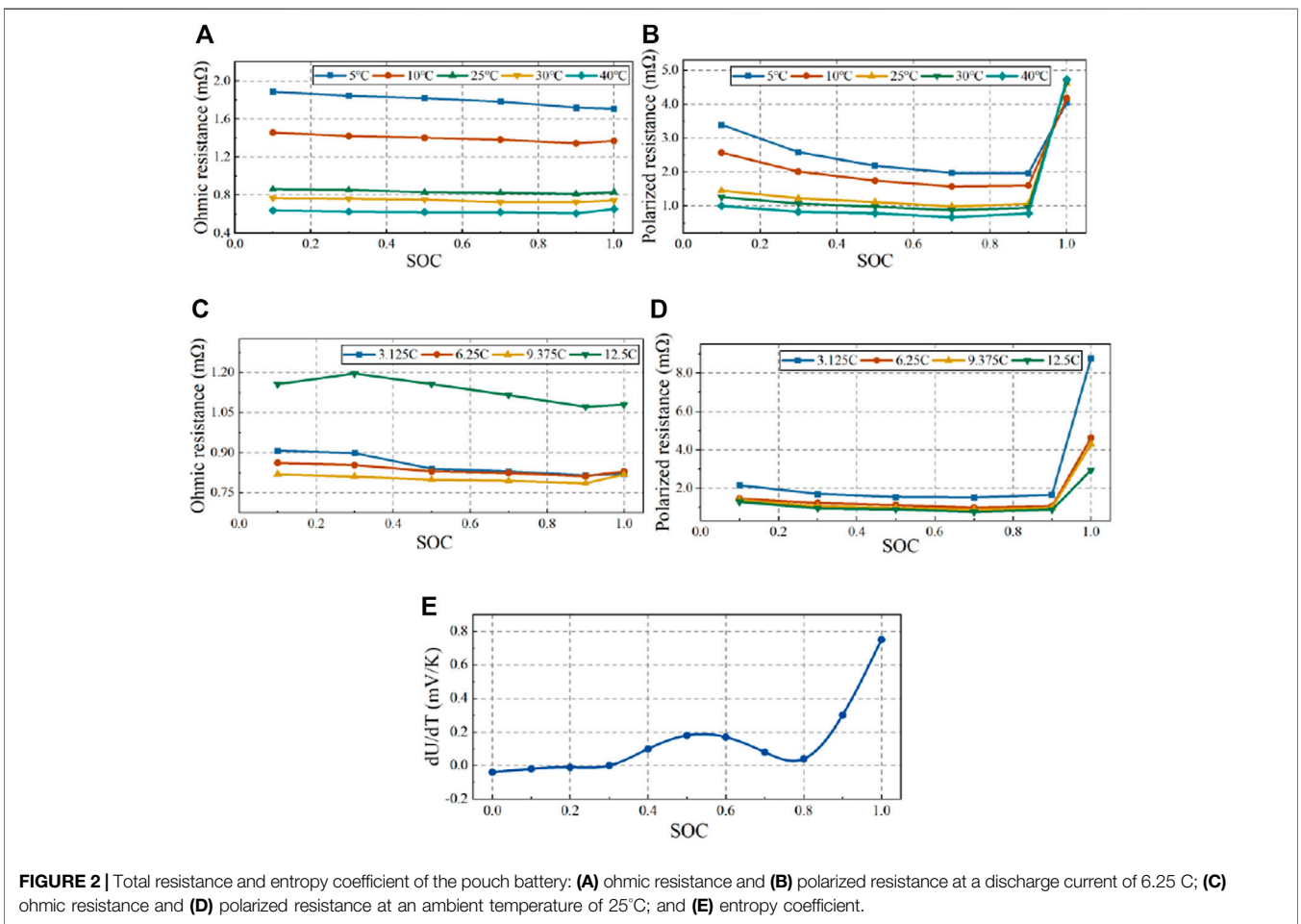$$+ D^{(2)}I \cdot T + D^{(3)}SOC \cdot T + E^{(1)} \quad (6)$$

$$R_p(I, SOC, T) = \sum_{i=1}^{4}A_i^{(2)}I^i + \sum_{i=1}^{4}B_i^{(2)}SOC^i + \sum_{i=1}^{4}C_i^{(2)}T^i + D^{(4)}I$$
$$\cdot SOC + D^{(5)}I \cdot T + D^{(6)}SOC \cdot T + E^{(2)} \quad (7)$$

where the coefficients are:

$$A = \begin{bmatrix} A_1^{(1)} & A_2^{(1)} & A_3^{(1)} & A_4^{(1)} \\ A_1^{(2)} & A_2^{(2)} & A_3^{(2)} & A_4^{(2)} \end{bmatrix}$$
$$= \begin{bmatrix} 0.0789 & -0.0012 & 5.433 \times 10^{-6} & 6.372 \times 10^{-9} \\ -0.0265 & 0.0001 & 0 & 0 \end{bmatrix} \quad (8)$$
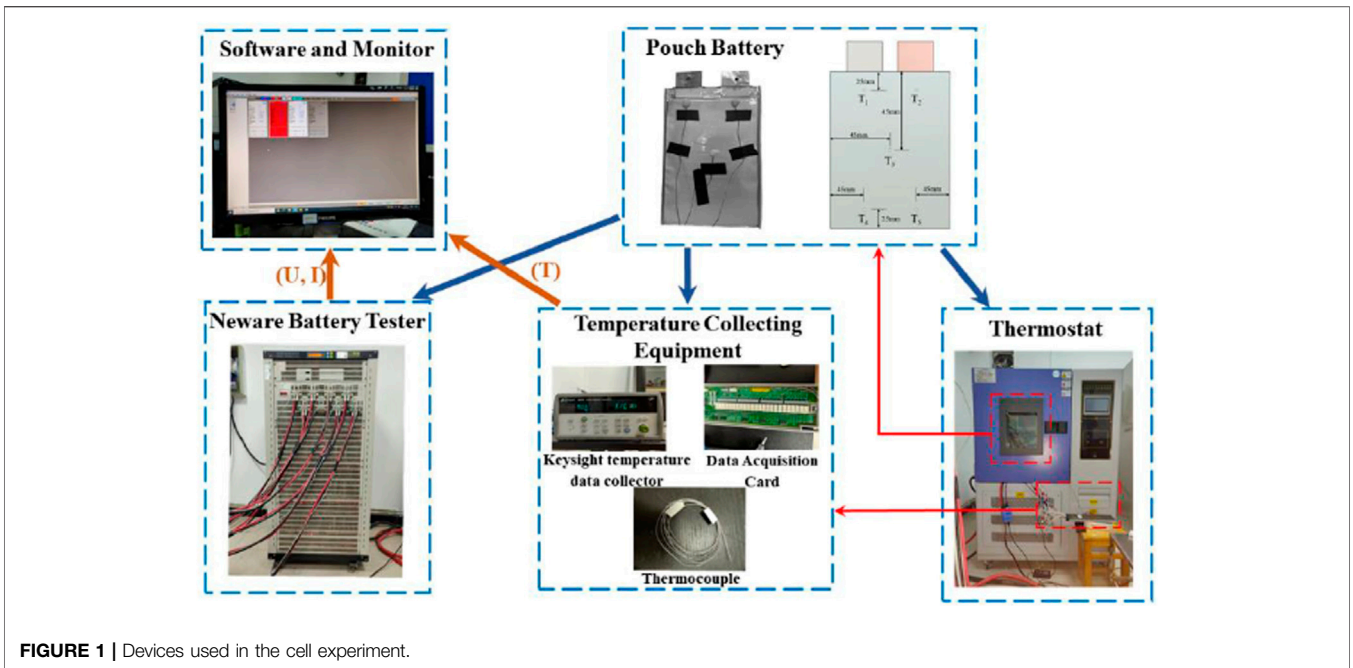
FIGURE 1 | Devices used in the cell experiment.

FIGURE 2 | Total resistance and entropy coefficient of the pouch battery: **(A)** ohmic resistance and **(B)** polarized resistance at a discharge current of 6.25 C; **(C)** ohmic resistance and **(D)** polarized resistance at an ambient temperature of 25°C; and **(E)** entropy coefficient.

$$B = \begin{bmatrix} B_1^{(1)} & B_2^{(1)} & B_3^{(1)} & B_4^{(1)} \\ B_1^{(2)} & B_2^{(2)} & B_3^{(2)} & B_4^{(2)} \end{bmatrix}$$
$$= \begin{bmatrix} -0.1297 & 0.1714 & -0.4099 & 0.2520 \\ -7.8572 & 19.978 & -26.182 & 12.656 \end{bmatrix} \tag{9}$$

$$C = \begin{bmatrix} C_1^{(1)} & C_2^{(1)} & C_3^{(1)} & C_4^{(1)} \\ C_1^{(2)} & C_2^{(2)} & C_3^{(2)} & C_4^{(2)} \end{bmatrix}$$
$$= \begin{bmatrix} -0.1137 & 0.0071 & -0.0002 & 2.256 \times 10^{-6} \\ -0.1617 & 0.0036 & -5.0897 & 2.587 \times 10^{-6} \end{bmatrix} \tag{10}$$

$$D = \begin{bmatrix} D^{(1)} & D^{(2)} & D^{(3)} \\ D^{(4)} & D^{(5)} & D^{(6)} \end{bmatrix} = \begin{bmatrix} -5.0910 & -0.0003 & 0.0028 \\ -0.0036 & 0.0002 & 0.0336 \end{bmatrix}$$
$$\tag{11}$$

$$E = \begin{bmatrix} E^{(1)} & E^{(2)} \end{bmatrix} = \begin{bmatrix} 0.3323 & 5.3399 \end{bmatrix}. \tag{12}$$

The correlation coefficient R^2 was applied to evaluate the fitting precision. Its values of 0.996 for ohmic resistance and 0.98 for polarization resistance indicate that **Eqs 6, 7** are accurate enough to predict the battery resistance at high current rates.

The evolution in the **Figure 2E**. A seventh-order PRSM was applied to fit the data, and the relationship between the entropy coefficient and SOC is:

$$\frac{dU_{OCV}}{dT}(SOC) = \sum_{i=0}^{8} p_i SOC^{i-1} \tag{13}$$

where

$$p_i = [-198.77, \ 630.36, \ -744.55, \ 404.24, \ -100.83, \ 10.42,$$
$$-0.1533, \ -0.04014].$$

The R^2 value of **Eq. 14** is 0.993, indicating that this equation is accurate enough to predict the entropy coefficient.

2.2.2 Resistance of Tabs

The parameter identification method was used to obtain the total resistance $R_{tab,j}$ and heat transfer coefficient $h_{tab,j}$. From **Eq. 4**, $\Delta T_{tab,j}$ can be expressed as:

$$\Delta T_{\text{tab},j} = -\frac{I^2 R_{\text{tab},j}}{h_{\text{tab},j} A_{\text{tab},j}} e^{-\frac{h_{\text{tab},j} A_{\text{tab},j}}{m_{tab,j} C_{p,tab,j}} t} + \frac{I^2 R_{\text{tab},j}}{h_{\text{tab},j} A_{\text{tab},j}}. \tag{14}$$

The variation curve of calculated $\Delta T_{\text{tab},j}$ values over times acquired from **Eq. 14** is fitted with the experimentally measured values by adjusting the total resistance $R_{\text{tab},j}$ and heat transfer coefficient $h_{\text{tab},j}$. Once the identified $\Delta T_{\text{tab},j}$ curve agreed with the tested one, the $R_{\text{tab},j}$ and $h_{\text{tab},j}$ values were determined. For the pouch battery, the $R_{\text{tab},p}$, $R_{\text{tab},n}$ and h_t values were 0.198 mΩ, 0.027 mΩ and 5.7 W/m²•K, respectively.

2.2.3 Physical Parameters

According to **Eq. 1**, the specific heat capacity C_p, density ρ, and thermal conductivities k_x, k_y and k_z should be modelled in order to predict the temperature distribution inside the cell. The lumped parameter method was used for modelling, which can be expressed as:

$$\rho_i = \frac{\sum m_i}{\sum v_i} \tag{15}$$

$$C_p = \frac{\sum m_i C_{pi}}{\sum m_i} \tag{16}$$

$$k_x = \frac{\sum L_i k_i}{\sum L_i} \tag{17}$$

$$k_y = \frac{\sum L_i}{\sum \frac{L_i}{k_i}} \tag{18}$$

$$k_z = \frac{\sum L_i k_i}{\sum L_i} \tag{19}$$

where m is the material mass, v is the material volume, ρ is the material density, L is the material thickness, k is the thermal conductivity of the material, and subscript i represents the type of material. **Supplementary Table S1** in the appendix gives the geometrical and physical parameters of the cell for **Eqs (15) to 19**).

2.3 Cell Thermal Model Verification

An experiment using the devices shown in **Figure 1** was carried out to validate the thermal model of the cell. The discharge currents used for verification were 6.25, 9.375 and 12.5°C, and the ambient temperatures were 17°C, 27°C and 37°C. Finite element method (FEM) was used to solve the thermal models created in this paper, and ANSYS Fluent is used as the solver. Firstly, the cell structure was constructed using CATIA, and then the geometric models were imported into ANSA for geometric pre-processing and meshing. A hexahedral grid was adopted to discretize the computational domain due to the regular structure of the pouch battery geometric model shown in **Figure 3A**, and its number was determined to be 0.22 million after verification of the independence of the grid to the temperature change, as shown in **Figure 3B**. The number of grids ranges from 0.046 million to 0.94 million was tested with loading9.375°C currents under the ambient temperature of 27°C, and when it was greater than 0.22 million, the average temperature change was within 0.1°C.

The thermal boundary used for the cell thermal model is (Yang and Tao, 2006):

$$-k\left(\frac{\partial T}{\partial n}\right)_w = h\left(T_w - T_f\right) \tag{20}$$
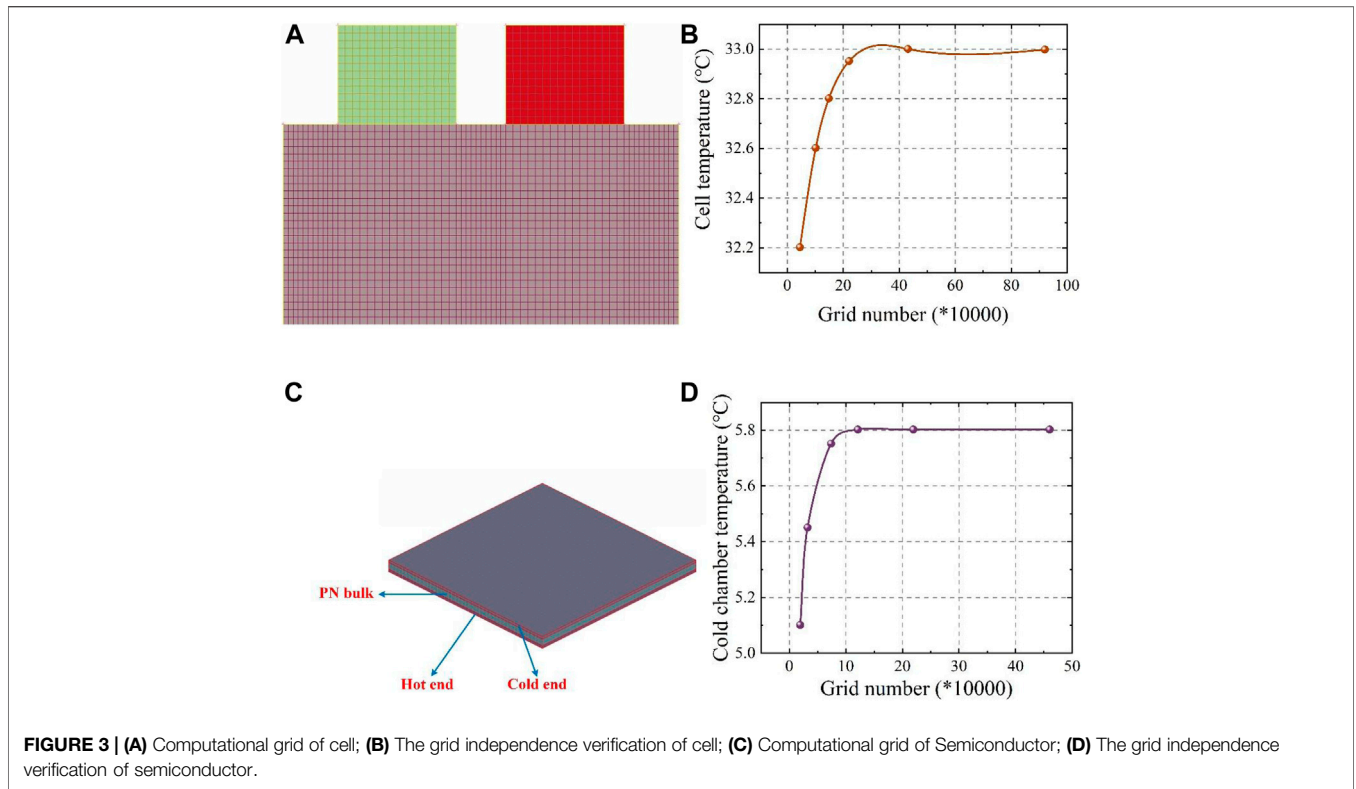
where T_w is the temperature on the cell surface, T_f is the air temperature near the cell, and h is the thermal transfer coefficient, which is calculated by:

$$h = \frac{Nu\lambda}{l} = 0.664 Re^{1/2} Pr^{1/3} \frac{\lambda}{l} \tag{21}$$

where the average Nusselt number Nu indicates the intensity of convective heat transfer, λ is the thermal conductivity of air, l is the characteristic length, and Pr is the Prandtl number, Re is the Reynolds number, it can be expressed as:

$$Re = \frac{ul}{v} \tag{22}$$

where u is wind speed, v is the air viscosity coefficient. therefore, the thermal transfer coefficient is:

FIGURE 3 | (A) Computational grid of cell; **(B)** The grid independence verification of cell; **(C)** Computational grid of Semiconductor; **(D)** The grid independence verification of semiconductor.

$$h = \frac{0.664\lambda u^{1/2} Pr^{1/3}}{v^{1/2} l^{1/2}} \quad (23)$$

The anemometer was used to measure the wind speed of 0.9 m/s on the surface of the cell in the thermostat, and the physical parameters of the air at 27°C were brought into **Equation 23**, therefore, $h = 9.34 \; W/(m^2 \cdot k)$.

Figure 4 shows the temperature evolutions according to the experiment and simulation. The temperature behaviour predicted by the cell thermal model fitted well with the experimental measurements. The average absolute error (AE_{ave}) was used to evaluate the predictive accuracy of the model, and is expressed as:

$$AE_{ave} = \frac{1}{N} \sum_{i=1}^{N} \left| T_{s,i} - T_{e,i} \right| \quad (22a)$$

Table 2A shows the AE_{ave} values under different conditions. The majority of AE_{ave} values were below 0.8 C; therefore, the cell thermal model can accurately predict the thermal behaviour of the cell.

3 THERMAL MODEL OF THE BTMS

3.1 Heat Generation Model of Semiconductor

The TEC consisted of a number of p- and n-type semiconductor couples connected electrically in series and thermally in parallel. With the consumption of electrical energy, heat is transferred from one side of the device to the other side against a temperature

gradient (from cold to hot). The TEC operating principle is shown in **Figure 5A**. These couples were sandwiched between two thermally conductive and electrically insulated substrates. The heat direction could be altered by changing the polarity of the DC charging current so that the TEC could also be used as a temperature controller that either heats or cools. The physical effects of semiconductor refrigeration mainly include three reversible effects—the Seebeck, Parr paste and Thomson effects—and two irreversible effects—the Joule and Fourier effects. Thus, the heat generation rate of the TEC can be expressed as:

$$q_c = \frac{I\alpha_{pn}T_c}{V_c} \quad (23a)$$

$$q_b = \frac{I^2 R_s}{V_b} \quad (24)$$

$$q_h = \frac{I\alpha_{pn}T_h}{V_h} \quad (25)$$

where q is the heat generation rate; I is the current through the semiconductor; R_s is the resistance of the semiconductor; α_{pn} is the Seebeck coefficient; T is the temperature of the semiconductor; and V is volume. The subscripts c, b and h represent the cold end, PN bulk, and hot end, respectively.

3.1.1 Parameters of the Semiconductor Model

The resistance R_s and Seebeck coefficient α_{pn} are required for calculation of the heat production rate. The TEC materials were assumed to be isotropic with constant physical parameters that did not vary with temperature. The 72,001/241/060B type of
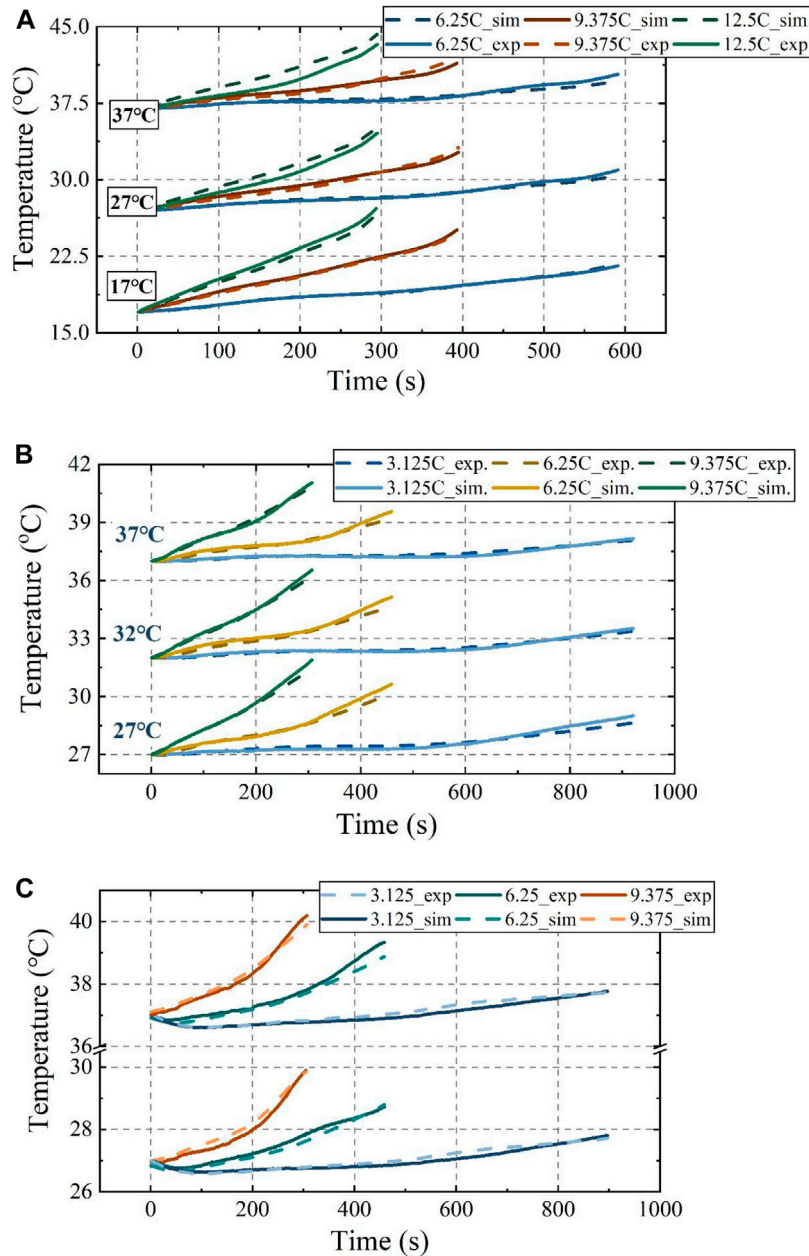
FIGURE 4 | Thermal model validation at different currents and ambient temperatures: **(A)** Cell thermal model; **(B)** Battery pack thermal model; **(C)** BTMS thermal model.

semiconductor was applied in this paper and its main parameters are shown in **Table 3**.

Figure 5B shows the structure of the TEC and its dimensions are shown in **Supplementary Table S2** of appendix. The whole system was powered by a 12 V electric source. Both conduction fins at the cold and hot ends were turned on to cool the closed chamber made of polyurethane insulation board material. The temperature of the semiconductor was recorded by the temperature sensors. The arrangement of the measurement points is shown in **Figure 5B**.

Different currents were loaded on the semiconductor at an ambient temperature of 27°C and the experimental results are shown in **Supplementary Table S3**. The TEC operating voltage is equal to the sum of the voltage drop generated by the resistance of the semiconductor and the Seebeck voltage:

$$U = IR_s + \alpha_{pn}\Delta T = IR_s + \alpha_{pn}(T_h - T_c) \tag{26}$$

Parameters R_s and α_{pn} were calculated to be 1.8 Ω and 0.065 V/K, respectively.

TABLE 2 | AE_{ave} values of different thermal models (°C). (Panel A) Cell thermal model (Panel B) Semiconductor thermal model (Panel C) Battery pack thermal model(Panel D) BTMS thermal model.

Current (C)	17°C	27°C	37°C
6.25	0.05	0.13	0.19
9.375	0.12	0.25	0.26
12.5	0.38	0.58	0.86

Current (A)	Hot end		Cold end
1.6	0.87		1.20
2.4	1.03		1.30
3.2	0.54		0.69
4	1.37		0.78

Cell number	Current (C)	27°C	32°C	37°C
2	3.125	0.09	0.07	0.11
	6.25	0.13	0.25	0.09
	9.375	0.12	0.14	0.08
7	3.125	0.12	0.11	0.06
	6.25	0.13	0.44	0.10
	9.375	0.14	0.23	0.07
13	3.125	0.10	0.08	0.08
	6.25	0.10	0.13	0.08
	9.375	0.12	0.08	0.06

Cell number	Current (C)	27°C	37°C
2	3.125	0.15	0.15
	6.25	0.17	0.23
	9.375	0.24	0.31
7	3.125	0.13	0.15
	6.25	0.14	0.17
	9.375	0.20	0.26
13	3.125	0.13	0.16
	6.25	0.17	0.19
	9.375	0.20	0.24

3.1.2 Verification of the Semiconductor Thermal Model

The FEM method was also applied to the validation of the semiconductor thermal model with a grid number of 121,000 after grid-independent verification. Its computational grid and verification are shown in **Figures 3C,D**. The temperature evolution in the simulation and experiment at different currents are shown in **Figure 6** for the AE_{ave} values in **Table 2B**. The simulation and experiment data fitted well with a maximum AE_{ave} of 1.30°C; thus, the temperature performance of semiconductor can be concisely described by the thermal model. Compared with other conditions, the temperature at the cold end approached 0°C and remained stable when the semiconductor was loaded with a current of 3.2 A. An increase in current led to an elevated temperature at the hot end, weakening the cooling performance of the TEC system. Therefore, 3.2 A was selected as the appropriate operating current for the semiconductor in this paper.

3.2 Thermal Model of the SBTMS

In the SBTMS, the total heat transfer process is divided into four parts. The first part is the heat conduction between the cell and aluminium heat dissipation structure. The heat generated by the cell is transferred to the base through graphene and heat-conducting fins, or the contact surface between the bottom of the cell and the base. The heat transfer inside the cell was modelled in **Section 2**. Assuming that the thermal conductivity of the graphene and aluminium plate are constant, the thermal conductivity equation for this process is:

$$\frac{\partial T}{\partial t} = a\left(\frac{\partial^2 T}{\partial x^2} + \frac{\partial^2 T}{\partial y^2} + \frac{\partial^2 T}{\partial z^2}\right) \tag{26a}$$

where a is the thermal diffusion coefficient, which can be expressed as:

$$a = k_m / \rho_m C_{p,m} \tag{27}$$

Subscript m represents the thermal conductivity media (aluminium plates and graphene) parameters.

The second part is the heat transfer between the cold end and hot end. The heat of the aluminium base is absorbed by the cold end and transferred to the hot end by the semiconductor cooling effect, which was modelled in **Section 3.1**. The heat transfers from the surface of the heat-conducting fins to the air at the hot end and the heat transfer in the air are the third part and the fourth part, respectively. The governing equations are used for these processes are:

1 Mass conservation equation, assuming that the density of incompressible fluids is constant, it can be simplified as:

$$\frac{\partial(\rho u)}{\partial x} + \frac{\partial(\rho v)}{\partial y} + \frac{\partial(\rho w)}{\partial y} = 0 \tag{28}$$

Where t is the time, ρ is the fluid density, u, v, w are the velocity vector of the fluid in x, y, z directions, respectively.

2 Momentum conservation equation:

$$\frac{\partial(\rho u)}{\partial t} + \nabla \cdot \left(\rho u \vec{u}\right) = -\frac{\partial P}{\partial x} + \frac{\partial \tau_{xx}}{\partial x} + \frac{\partial \tau_{yx}}{\partial y} + \frac{\partial \tau_{zx}}{\partial z} + F_x \tag{29}$$

$$\frac{\partial(\rho v)}{\partial t} + \nabla \cdot \left(\rho v \vec{u}\right) = -\frac{\partial P}{\partial y} + \frac{\partial \tau_{xy}}{\partial x} + \frac{\partial \tau_{yy}}{\partial y} + \frac{\partial \tau_{zy}}{\partial z} + F_y \tag{30}$$

$$\frac{\partial(\rho w)}{\partial t} + \nabla \cdot \left(\rho w \vec{u}\right) = -\frac{\partial P}{\partial z} + \frac{\partial \tau_{xz}}{\partial x} + \frac{\partial \tau_{yz}}{\partial y} + \frac{\partial \tau_{zz}}{\partial z} + F_z \tag{31}$$

where P is the static pressure, τ_{xx}, τ_{yx}, τ_{zx} is the viscous stress in the x, y and z directions, F_x, F_y, F_z is the gravity in the x, y and z directions.

3 Energy conservation equation

$$\frac{\partial t}{\partial \tau} + u\frac{\partial t}{\partial x} + v\frac{\partial t}{\partial y} + w\frac{\partial t}{\partial z} = \frac{\lambda}{\rho c_p}\left(\frac{\partial^2 t}{\partial x^2} + \frac{\partial^2 t}{\partial y^2} + \frac{\partial^2 t}{\partial x^2}\right) \tag{32}$$

4 $k - \varepsilon$ turbulence model

The fluid flow under turbulent conditions is unstable. In this paper, $k - \varepsilon$ turbulence model was selected to describe the fluid condition according to the requirements of calculation rate and solution accuracy, in which the k is the turbulent energy and the ε is the turbulent dissipation rate. The turbulent viscosity μ_t can be expressed as
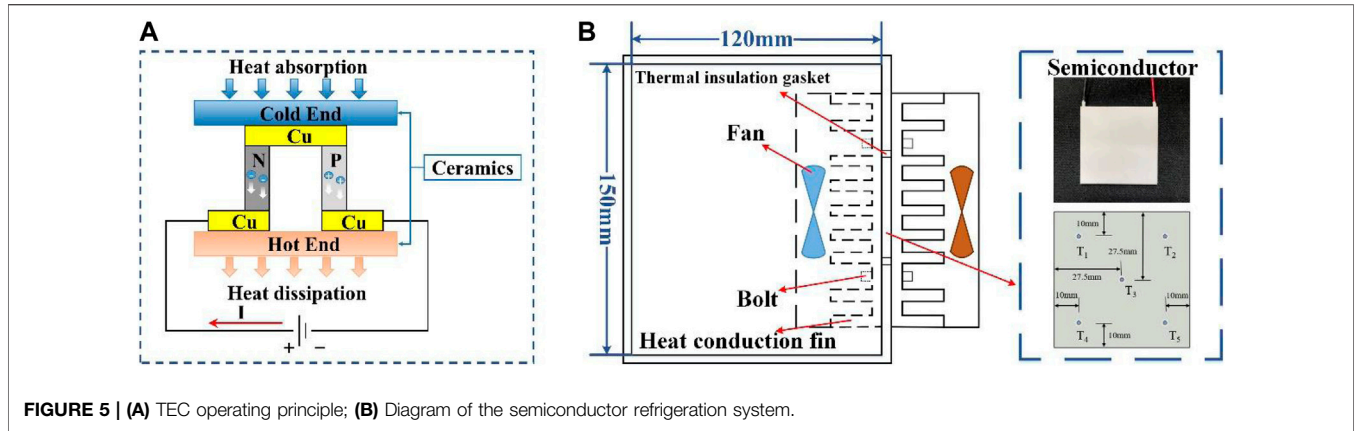
FIGURE 5 | (A) TEC operating principle; (B) Diagram of the semiconductor refrigeration system.

$$\mu_t = \rho C_\mu \frac{k^2}{\varepsilon} \qquad (33)$$

The standard $k - \varepsilon$ turbulence model is:

$$\frac{\partial(\rho k)}{\partial t} + \frac{\partial(\rho k u_i)}{\partial x_i} = \frac{\partial}{\partial x_j}\left[\left(\mu + \frac{\mu_i}{\sigma_k}\right)\frac{\partial k}{\partial x_j}\right] + G_k + G_b - \rho\varepsilon - Y_M$$
$$+ S_k \qquad (34)$$

$$\frac{\partial(\rho\varepsilon)}{\partial t} + \frac{\partial(\rho\varepsilon u_i)}{\partial x_i} = \frac{\partial}{\partial x_j}\left[\left(\mu + \frac{\mu_i}{\sigma_\varepsilon}\right)\frac{\partial\varepsilon}{\partial x_j}\right] + C_{1\varepsilon}\frac{\varepsilon}{k}(G_k + C_{3\varepsilon}G_b)$$
$$- C_{2\varepsilon}\rho\frac{\varepsilon^2}{k} + S_\varepsilon \qquad (35)$$

where G_k, G_b is the turbulent kinetic energy, can be calculated as:

$$G_k = \mu_t \frac{\partial\mu_i}{\partial x_j}\left(\frac{\partial\mu_i}{\partial x_j} + \frac{\partial\mu_j}{\partial x_i}\right) \qquad (36)$$

where Y_M is the pulsation expansion item; $C_{1\varepsilon}$, $C_{2\varepsilon}$ and $C_{3\varepsilon}$ are empirical constants; σ_k and σ_ε represent the Prandtl number of k and ε, respectively; S_k and S_ε are source items.

5 Fluid-solid coupled heat transfer model

In numerical simulations, the fluid-solid coupling interface must be coupled to the interface surface mesh in order to achieve the interaction of heat transfer data, in other words, to achieve the one-to-one correspondence of the interface mesh nodes. Based on the basic theorem of convective heat transfer, the governing equation at the fluid-solid contact interface is:

$$c = \frac{dz_f}{dz_s} \qquad (37)$$

$$\left(k\frac{\partial T}{\partial z}\right)_f = \left(k\frac{\partial T}{\partial z}\right)_s \qquad (38)$$

$$T_{S-F} = \frac{ck_S T_S + k_f T_f}{ck_S + k_f} \qquad (39)$$

where c is the ratio of the distance between the center of the solid (z_s) and fluid (z_f) grid micro-element, k_S is the thermal conductivity of the solid, and T_S is the temperature of the solid, and T_{S-F} is the temperature of the fluid-solid cross-interface.

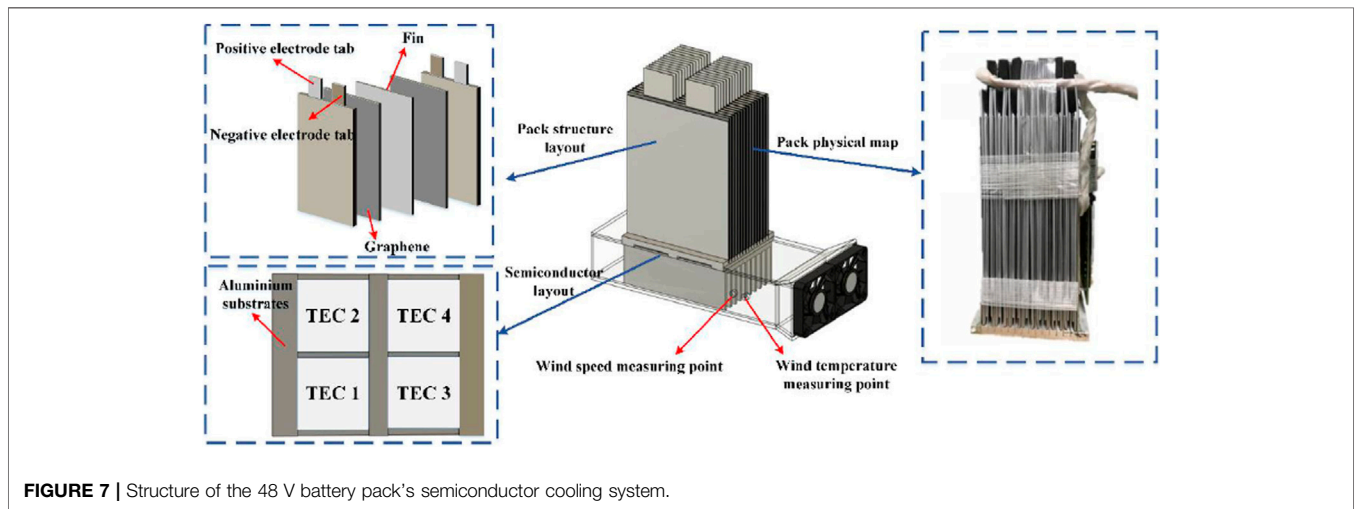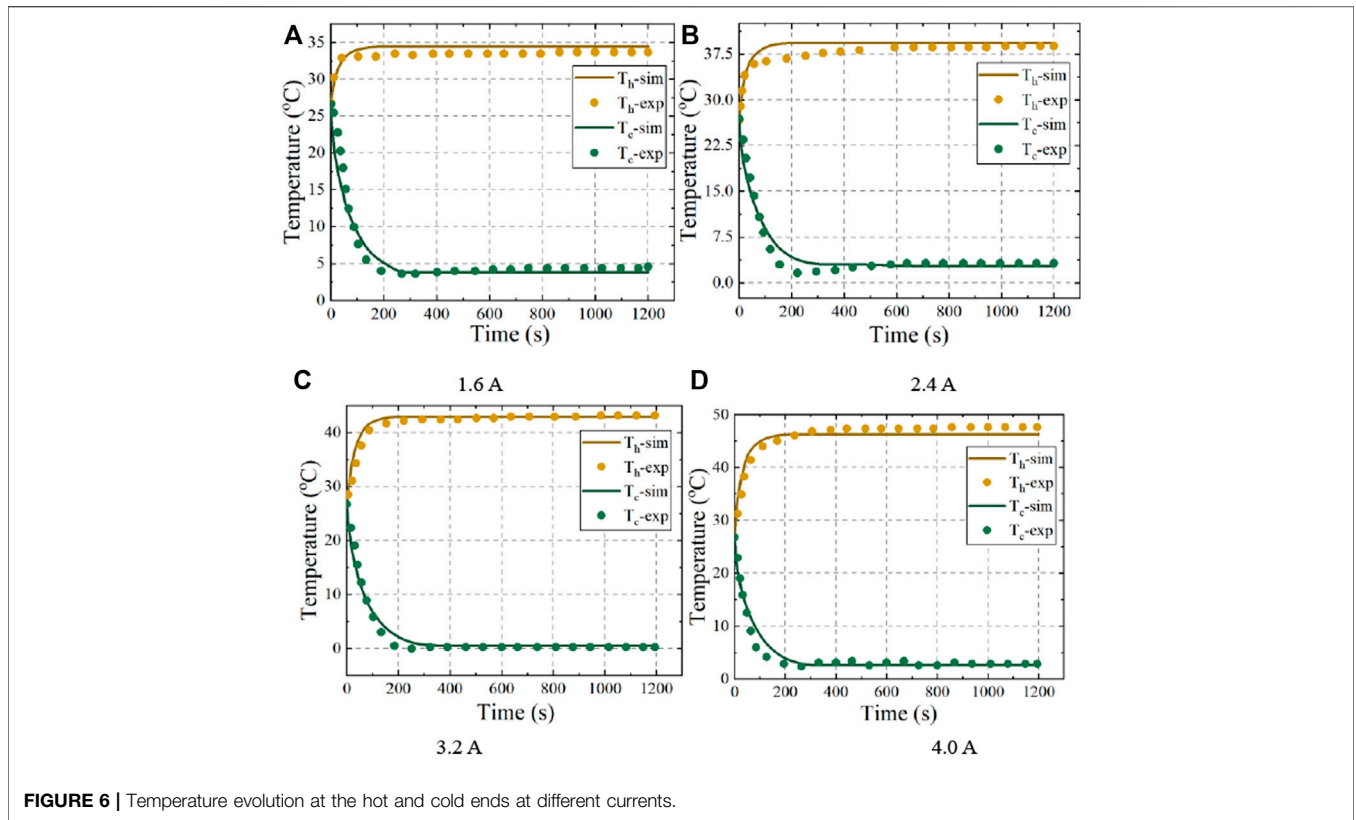# 4 THERMAL BEHAVIOUR OF THE SBTMS

4.1 Structure of the SBTMS

The overall structure of the 48 V battery pack based on TEC is shown in **Figure 7**. The thickness of the heat-conducting fins and graphene were 1 and 0.6 mm, respectively, and an aluminium slot base with a depth of 5 mm fixed and supported the fins. Four semiconductors were embedded in a recess at the bottom of the aluminium base and held in place with thermally conductive silicone. Two 80 × 80 mm fans were used for forced-air cooling of the fins at the hot end and two holes of 10 mm diameter were reserved on the air duct side to measure the temperature and speed of the airflow. The parameters of the 48 V battery pack are shown in **Table 1**.

4.2 Computation and Simulation Setups

The computational fluid dynamics (CFD)-based method was used to solve the 48 V battery pack BTMS model. The governing equations were discretized by the FEM using a hexahedral grid for the battery pack and semiconductor and a

TABLE 3 | Physical parameters of the semiconductor (T_h = 50°C).

Parameter	Value
Size (mm)	55 × 55 × 3.50
I_{max} (A)	6.0
U_{max} (V)	34.3
ΔT_{max} (°C)	83
Q_{max} (W)	108
Density of cold/hot end (kg/m³)	2,900
Density of PN bulk (kg/m³)	10,922
Specific heat capacity of cold/hot end (J·kg⁻¹·K⁻¹)	419
Specific heat capacity of PN bulk (J·kg⁻¹·K⁻¹)	200
Heat transfer coefficient of cold/hot end (W·m⁻¹·K⁻¹)	18.5
Heat transfer coefficient of PN bulk (W·m⁻¹·K⁻¹)	2

FIGURE 6 | Temperature evolution at the hot and cold ends at different currents.

FIGURE 7 | Structure of the 48 V battery pack's semiconductor cooling system.

tetrahedral grid for the fins and fluid region with a most suitable grid number of five million, as shown in **Figure 8A**. The discretization method used for the governing equations is shown in **Table 4**, and the physical parameters of the materials in the cooling system are shown in **Supplementary Table S4**. **Figure 8B** shows the boundary conditions and computational domain of the SBTMS.

4.3 SBTMS Thermal Model Verification

To verify the accuracy of the model, the battery pack was discharged from SOC = 0.9 to 0.1 at ambient temperatures of 27°C, 32°C and 37°C and discharge currents of 3.125, 6.25, 9.375 and 12.5°C. In the experiments, the surface of the battery pack was wrapped adiabatically and temperature sensors were attached to the centres of the two sides.
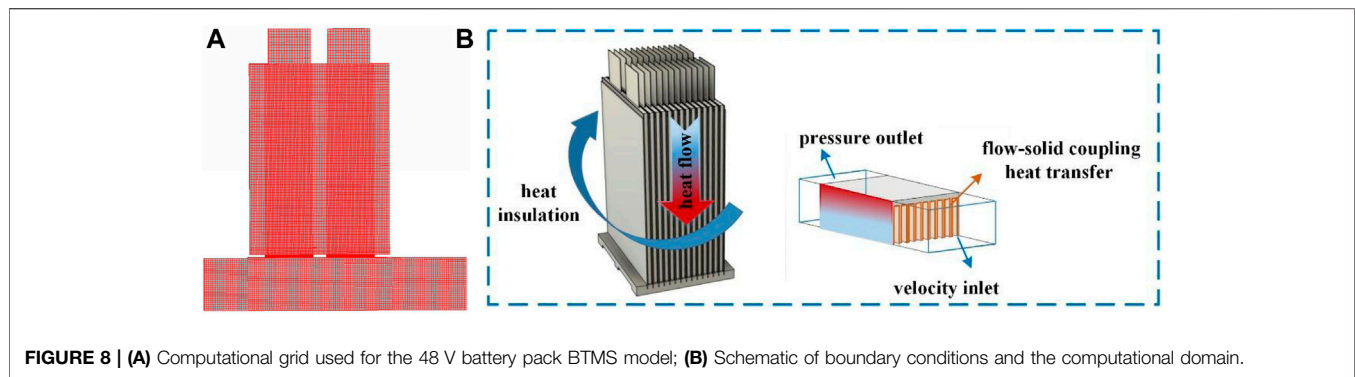
FIGURE 8 | (A) Computational grid used for the 48 V battery pack BTMS model; **(B)** Schematic of boundary conditions and the computational domain.
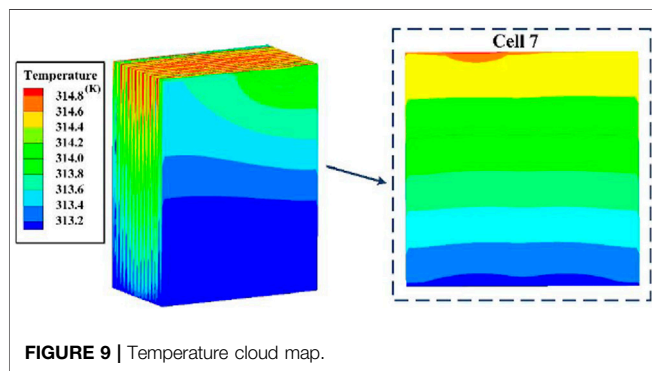
FIGURE 9 | Temperature cloud map.

4.3.1 Battery Pack
1 Temperature evolution

The T_1 point of battery No. 7 was the highest among all temperature measurement points in the battery pack, and using the temperature of this point as an example, the temperature evolution in the experiment and simulation at current loadings of 3.125, 6.25 and 9.375 C from 27°C to 37°C were highly consistent, with a majority of AE_{ave} values being below 0.15°C, as shown as **Figure 4B** and **Table 2C**. Therefore, the thermal model can effectively simulate the temperature variation in the 48 V battery pack.

2 Temperature distribution

A simulated temperature cloud map of a battery pack at the end of discharge can be used to show its temperature distribution visually. In **Figure 9**, when the battery pack was discharged at an ambient temperature of 37°C and current of 9.375 C, its temperature decreased from the top (near the tabs) to the bottom. The cells located in the middle of the pack had higher temperatures than those on the two sides, which is consistent with the theoretical analysis. The heat production rate of the positive electrode tab material (Al) was higher than that of the negative electrode tab (Cu), and the heat conduction from top to bottom was not an instantaneous process, so the maximum temperature occurred in the area of the positive tab in the upper part of the

battery. Therefore, the temperature of the battery pack was chosen to be the measurement point temperature closest to the battery tab when BTMS was applied. The reliability of BTMS can be demonstrated if the maximum temperature of the battery pack was controlled within the appropriate range. Graphene with good temperature homogenisation provides a small temperature difference within each cell, and the maximum temperature difference within the cell did not exceed 2 C. However, the heat transfer coefficient of both the pouch lithium battery and graphene in the lateral direction were much smaller than those in the longitudinal and axial directions, making heat accumulate in the middle of the pack more easily. In addition, the maximum temperature of the battery was already over 40°C when a current of 9.375 C was loaded in the pack at an ambient temperature of 37°C. As the current continues to increase, the temperature of the battery will increase, seriously affecting its performance and cycle life, and temperature differences in different locations inside the cell and temperature inconsistency between cells will gradually increase.

4.3.2 Semiconductor-Based BTMS
The 48 V battery pack was discharged at 3.123, 6.25 and 9.375 C currents at a 37°C and 27°C ambient temperature, and the semiconductor-based BTMS was turned on to test the cooling effect of the semiconductor at a current of 2.0 A and an airflow speed of 5 m/s. The T_1 point of battery No. 7 was selected as the temperature monitoring point for its maximum temperature character in the BTMS model verification. As shown in **Figure 4C**, the simulations and experiments were more accurately fitted in the early stage of discharge when the battery temperature was low, while the error increased in the late stage of discharge at 9.375°C, with the simulated temperatures being lower than the measured ones. This is due to heat accumulation from the battery in the late discharge period; heat not readily transferred from the hot end will cause the cold-end temperature of the semiconductor to rise and decrease the cooling performance. However, the maximum error between the experiment and simulation was within 0.5°C and 0.3°C at 37°C and 27°C ambient temperature, respectively. And the majority of AE_{ave} in **Table 2D** are lower than 0.3°C, thus the semiconductor-based BTMS model can accurately estimate the temperature of the system.
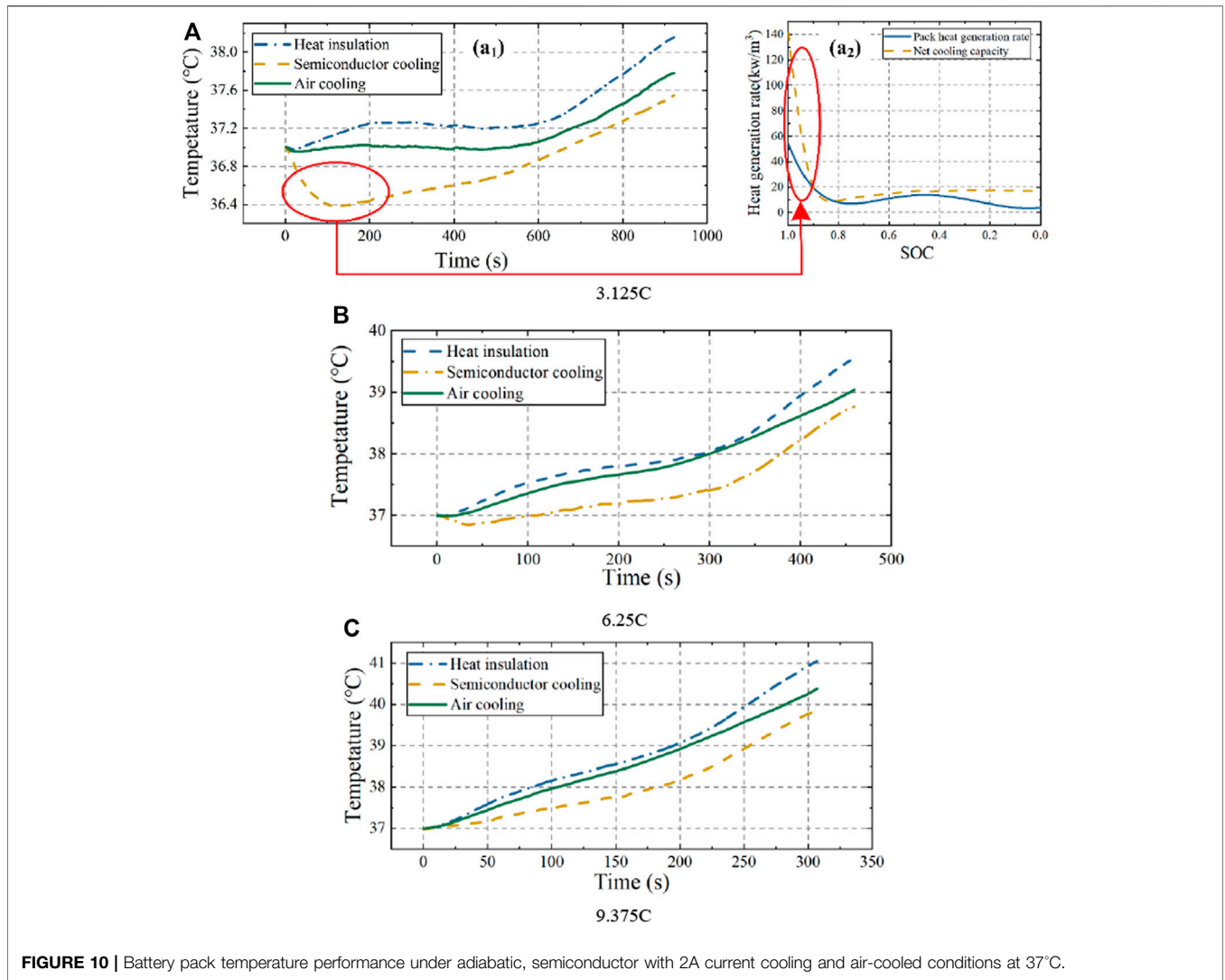
FIGURE 10 | Battery pack temperature performance under adiabatic, semiconductor with 2A current cooling and air-cooled conditions at 37°C.

4.4 Heat Dissipation of the SBTMS

The temperature evolution of the 48 V battery pack in the adiabatic state and with SBTMS at 2A current or air-cooled BTMS (ABTMS) were compared by discharging at constant currents of 3.125, 6.25, and 9.375 C, respectively, at 37°C, as shown in **Figure 10**. The temperature of the battery pack with SBTMS decreased at the beginning of discharge when loaded with 3.125 and 6.25 C currents, and was particularly noticeable at 3.125 C. The net cooling capacity of the semiconductor can be calculated as:

$$Q_0 = \alpha_{pn} T_c I - \frac{1}{2} I^2 R_s - K \Delta T \tag{40}$$

K is the semiconductor thermal resistance, ΔT is the temperature difference between the cold and hot end of the semiconductor.

The calculated heat generation rate of the battery pack loaded with 3.125C current and the TEC cooling rate of the battery pack loaded with 2A current as a function of the SOC (discharge time) at an ambient temperature of 37°C are shown in **Figure 10** (A_2). The TEC cooling rate was much higher than the heat production of the battery pack at the early stage of discharge, so that a significant temperature reduction of the battery pack occurs in **Figure 10** (A_1). However, this phenomenon disappeared when the pack was discharged at 9.375 C, when there was very high heat production.

Temperature decreases of 0.6°C, 0.78°C and 1.21°C at currents of 3.125, 6.25 and 9.375 C, respectively, were achieved in the battery pack with SBTMS. The maximum temperature of the pack at 9.375 C current was 39.84°C as shown in **Table 5**, and the maximum temperature difference between cells was 1.6°C, which meet the requirements for optimal pack operating temperature range and temperature consistency. However, if the current increases, the semiconductor-cooled battery pack will exceed the safe operating temperature. Therefore, loading the TEC with 2 A current was the minimum current at which

TABLE 4 | Discretization method for the governing equations.

Convection term	Pressure term	DiffusionTerm	Other terms	Pressure-velocity coupling algorithm
2nd order upwind Scheme	2nd scheme	Central difference Scheme	1st order upwind Scheme	semi-implicit method for pressure-linked equations scheme (SIMPLE)

TABLE 5 | Temperature at the end of discharge (^{o}C).

Discharge rate (C)	Heat insulation	ABTMS	SBTMS(2A)	SBTMS(3.2A)
3.125	38.15	37.78	37.55	36.21
6.25	39.55	39.04	38.77	37.45
9.375	41.05	40.38	39.84	38.82

SBTMS can achieve temperature control within 40°C of the pack at 9.375 C current and an ambient temperature of 37°C discharge. As the TEC current increases, the cooling effect increases and better demonstrates the superiority of the SBTMS.

For a battery pack with ABTMS, the temperature decreased by 0.37°C, 0.51°C and 0.67°C compared with the pack in the adiabatic state; hence, it had a weaker cooling effect than SBTMS. Moreover, the lower thermal inertia of semiconductors allows for higher cooling sensitivity. At currents of 3.125, 6.25 and 9.375 C, the pack with SBTMS achieved cooling of 0.2°C some 149 s, 67 s and 120 s faster, respectively, than the pack with ABTMS.

5 CONCLUSION

A semiconductor-based BTMS thermal model was developed to predict the temperature performance of a 48 V battery pack. It integrates a resistance-based cell thermal model, a semiconductor thermal model, and a three-dimensional fluid-solid coupled heat transfer model. The performance of the semiconductor cooling system at high temperatures and discharge rates was verified using this model and compared with that of an air-cooled system. Based on the results, the following conclusions are made.

1. The battery thermal model considers the effects of current, temperature and SOC on ohmic resistance and polarization resistance. It can accurately predict the thermal behaviour of 8 Ah pouch batteries. The maximum errors in temperature prediction by the thermal model were mostly <0.8°C at the cell level and <0.6°C at the pack level.
2. In this paper, a BTMS structure with coupled semiconductor and air cooling was designed. The proposed BTMS thermal model was able to accurately describe the temperature performance of the battery, with a maximum error within 0.5°C in ambient temperature of 37°C and 0.3°C in 27°C. At an ambient temperature of 37°C and high current rate (up to 9.375 C), the SBTMS achieved an overall temperature control requirement of <40°C and provided a temperature difference of no more than 1.6°C in the 48 V battery pack.
3. The hybrid semiconductor-based BTMS was more sensitive and had a better cooling effect than the single air-cooled BTMS. At 3.125, 6.25 and 9.375 C, the SBTMS achieved the initial 0.2°C temperature drop some 149 s, 76 s and 120 s faster, respectively, than the ABTMS and cooled the pack by 0.6°C, 0.78°C and 1.21 C at the end of discharge.

DATA AVAILABILITY STATEMENT

The original contributions presented in the study are included in the article/**Supplementary Material**, further inquiries can be directed to the corresponding author.

AUTHOR CONTRIBUTIONS

RY proposed the main idea of the paper, did the simulation and wrote the paper. KL, YX and WL built the battery thermal model. HZ did the experiment of 48 V. YQ and YZ dealt with the results of experiment and simulation, and checked the paper.

FUNDING

SUPPLEMENTARY MATERIAL

The Supplementary Material for this article can be found online at: https://www.frontiersin.org/articles/10.3389/fenrg.2021.794438/full#supplementary-material

REFERENCES

Al-Zareer, M., Dincer, I., and Rosen, M. A. (2017). Novel Thermal Management System Using Boiling Cooling for High-Powered Lithium-Ion Battery Packs for Hybrid Electric Vehicles. *J. Power Sourc.* 363, 291–303. doi:10.1016/j.jpowsour.2017.07.067

Alaoui, C., and Salameh, Z. M. (2005). A Novel Thermal Management for Electric and Hybrid Vehicles. *IEEE Trans. Veh. Technol.* 54 (2), 468–476. doi:10.1109/tvt.2004.842444

Alaoui, C., and Salameh, Z. M. (2003). "Modeling and Simulation of a Thermal Management System for Electric Vehicles," in 29th Annual Conference of the IEEE Industrial-Electronics-Society, Roanoke, VA, USA, 2-6 Nov. 2003, 887–890.

Bernardi, D., Pawlikowski, E., and Newman, J. (1985). A General Energy Balance for Battery Systems. *J. Electrochem. Soc.* 132 (1), 5–12. doi:10.1149/1.2113792

Bradley, T. H., and Quinn, C. W. (2010). Analysis of Plug-In Hybrid Electric Vehicle Utility Factors. *J. Power Sourc.* 195 (16), 5399–5408. doi:10.1016/j.jpowsour.2010.02.082

Dunn, B., Kamath, H., and Tarascon, J.-M. (2011). Electrical Energy Storage for the Grid: A Battery of Choices. *Science* 334 (6058), 928–935. doi:10.1126/science.1212741

Huang, Q., Li, X., Zhang, G., Zhang, J., He, F., and Li, Y. (2018). Experimental Investigation of the Thermal Performance of Heat Pipe Assisted Phase Change Material for Battery Thermal Management System. *Appl. Therm. Eng.* 141, 1092–1100. doi:10.1016/j.applthermaleng.2018.06.048

Ianniciello, L., Biwolé, P. H., and Achard, P. (2018). Electric Vehicles Batteries Thermal Management Systems Employing Phase Change Materials. *J. Power Sourc.* 378, 383–403. doi:10.1016/j.jpowsour.2017.12.071

Lee, S., Cherry, J., Safoutin, M., McDonald, J., and Olechiw, M. (2018). Modeling and Validation of 48V Mild Hybrid Lithium-Ion Battery Pack. *SAE Int. J. Alt. Power* 7 (3), 273–287. doi:10.4271/2018-01-0433

Li, X., Zhong, Z., Luo, J., Wang, Z., Yuan, W., Zhang, G., et al. (2019). Experimental Investigation on a Thermoelectric Cooler for Thermal Management of a Lithium-Ion Battery Module. *Int. J. Photoenergy* 2019, 1–10. doi:10.1155/2019/3725364

Liu, Y., Yang, S., Guo, B., and Deng, C. (2014). Numerical Analysis and Design of Thermal Management System for Lithium Ion Battery Pack Using Thermoelectric Coolers. *Adv. Mech. Eng.* 6, 852712. doi:10.1155/2014/852712

Lyu, Y., Siddique, A. R. M., Majid, S. H., Biglarbegian, M., Gadsden, S. A., and Mahmud, S. (2019). Electric Vehicle Battery Thermal Management System with Thermoelectric Cooling. *Energ. Rep.* 5, 822–827. doi:10.1016/j.egyr.2019.06.016

Maggetto, G., and Van Mierlo, J. (2001). Electric Vehicles, Hybrid Electric Vehicles and Fuel Cell Electric Vehicles : State of the Art and Perspectives. *Ann. de Chim. Sci. des Matériaux* 26 (4), 9–26. doi:10.1016/s0151-9107(01)80066-0

Malik, M., Dincer, I., and Rosen, M. A. (2016). Review on Use of Phase Change Materials in Battery Thermal Management for Electric and Hybrid Electric Vehicles. *Int. J. Energ. Res.* 40 (8), 1011–1031. doi:10.1002/er.3496

Pesaran, A. A. (2002). Battery Thermal Models for Hybrid Vehicle Simulations. *J. Power Sourc.* 110 (2), 377–382. doi:10.1016/S0378-7753(02)00200-8

Placke, T., Kloepsch, R., Dühnen, S., and Winter, M. (2017). Lithium Ion, Lithium Metal, and Alternative Rechargeable Battery Technologies: The Odyssey for High Energy Density. *J. Solid State. Electrochem.* 21 (7), 1939–1964. doi:10.1007/s10008-017-3610-7

Ran, B., Victor, A., and James, B. (2017). Effect of 48 V Mild Hybrid System Layout on Powertrain System Efficiency and its Potential of Fuel Economy Improvement. *SAE International. Technical Paper* 2017-01-1175. doi:10.4271/2017-01-1175

Seo, Y. M., Ha, M. Y., Park, S. H., Lee, G. H., Kim, Y. S., and Park, Y. G. (2018). A Numerical Study on the Performance of the Thermoelectric Module with Different Heat Sink Shapes. *Appl. Therm. Eng.* 128, 1082–1094. doi:10.1016/j.applthermaleng.2017.09.097

Seong Kim, U., Yi, J., Shin, C. B., Han, T., and Park, S. (2011). Modeling the Dependence of the Discharge Behavior of a Lithium-Ion Battery on the Environmental Temperature. *J. Electrochem. Soc.* 158 (5), A611–A618. doi:10.1149/1.3565179

Sirikasemsuk, S., Wiriyasart, S., Naphon, P., and Naphon, N. (2021). Thermal Cooling Characteristics of Li-Ion Battery Pack with Thermoelectric Ferrofluid Cooling Module. *Int. J. Energ. Res* 45 (6), 8824–8836. doi:10.1002/er.6417

Song, W., Bai, F., Chen, M., Lin, S., Feng, Z., and Li, Y. (2018). Thermal Management of Standby Battery for Outdoor Base Station Based on the Semiconductor Thermoelectric Device and Phase Change Materials. *Appl. Therm. Eng.* 137, 203–217. doi:10.1016/j.applthermaleng.2018.03.072

Stroe, D.-I., Swierczynski, M., Kar, S. K., and Teodorescu, R. (2018). Degradation Behavior of Lithium-Ion Batteries during Calendar Ageing-The Case of the Internal Resistance Increase. *IEEE Trans. Ind. Applicat.* 54 (1), 517–525. doi:10.1109/tia.2017.2756026

Tang, S., Wang, Z., Guo, H., Wang, J., Li, X., and Yan, G. (2019). Systematic Parameter Acquisition Method for Electrochemical Model of 4.35 V LiCoO2 Batteries. *Solid State Ionics* 343, 115083. doi:10.1016/j.ssi.2019.115083

Thomas, K. E., and Newman, J. (2003). Thermal Modeling of Porous Insertion Electrodes. *J. Electrochem. Soc.* 150 (2), A176–A192. doi:10.1149/1.1531194

Xie, Y., He, X.-J., Hu, X.-S., Li, W., Zhang, Y.-J., Liu, B., et al. (2020). An Improved Resistance-Based thermal Model for a Pouch Lithium-Ion Battery Considering Heat Generation of Posts. *Appl. Therm. Eng.* 164, 114455. doi:10.1016/j.applthermaleng.2019.114455

Yang, F., Ding, J., Huang, W., Xie, W., and Liu, W. (2014). Particle Size-Specific Distributions and Preliminary Exposure Assessments of Organophosphate Flame Retardants in Office Air Particulate Matter. *Environ. Sci. Technol.* 48 (1), 63–70. doi:10.1021/es403186z

Yang, S. M., and Tao, W. Q. (2006). *Heat Transfer*. Beijing,China: Higher Education Press.

Yu, C., Ji, G., Zhang, C., Abbott, J., Xu, M., Ramaekers, P., et al. (2018). Cost-Efficient Thermal Management for a 48V Li-Ion Battery in a Mild Hybrid Electric Vehicle. *Automot. Innov.* 1 (4), 320–330. doi:10.1007/s42154-018-0043-7

NOMENCLATURE

ρ battery density (kg/m^3)

C_p specific heat capacity (J/(kg· K))

T battery temperature (°C)

t time (s)

k_x thermal conductivities in the x-direction (W/(m· k))

k_y thermal conductivities in the y-direction (W/(m· k))

k_z thermal conductivities in the z-direction (W/(m· k))

q heat production rate (W/m^3)

Q_{total} total heat generation rate (W/m^3)

I Current (A)

V terminal voltage (V)

U open circuit voltage (V)

dU/dT entropy coefficient

R_o ohmic resistance (Ohm)

R_p polarized resistance (Ohm)

V_b cell volume (m^3)

$R_{tab,j}$ total resistance of the tab (Ohm)

R_c contact resistance (Ohm)

R_t tab resistance (Ohm)

m_{tab} tab mass (kg)

$C_{p,tab}$ specific heat capacity of tab (J/(kg· K))

T_{tab} tab temperature (°C)

h_{tab} heat transfer coefficient between the tab and the air

A_{tab} tab area (m^2)

ΔT_{tab} difference between the tab and ambient temperatures (°C)

$V_{tab,j}$ tab volume (m^3)

R^2 correlation coefficient

T_w cell surface temperature (°C)

T_f air temperature (°C)

h thermal transfer coefficient (W/(m^2· k))

Nu Nusselt number

λ thermal conductivity of air (W/(m· k))

l characteristic length (m)

Re Reynolds number

Pr Prandtl number

AE_{ave} average absolute error

R_s semiconductor resistance (Ohm)

α_{pn} Seebeck coefficient

q_c cold end heat generation rate (W/m^3)

q_b PN bulk heat generation rate (W/m^3)

q_h hot end heat generation rate (W/m^3)

p static pressure (Pa)

u, v, w velocity vector in the x, y and z directions (m/s)

$\tau_{xx}, \tau_{yx}, \tau_{zx}$ viscous stress in the x, y and z directions (N/m)

F_x, F_y, F_z gravity in the x, y and z directions (N)

k_s thermal conductivity (W/(m· k))

k turbulent kinetic energy (m^2/s^2)

ε turbulent kinetic energy dissipation rate

μ_t turbulent viscosity (m^2/s)

G_k, G_b turbulent kinetic energy (m^2/s^2)

Y_M pulsation expansion item

$C_{1\varepsilon}, C_{2\varepsilon}, C_{3\varepsilon}$ empirical constants

σ_k Prandtl number of turbulent kinetic energy

σ_ε Prandtl number of turbulent kinetic energy dissipation rate

S_k, S_ε source item

c ratio of the distance between the center of the solid (z_s) and fluid (z_f) grid micro-element

T_S Solid temperature (°C)

T_{S-F} fluid-solid cross-interface temperature (°C)

K semiconductor thermal resistance(Ohm)

ΔT temperature difference between the cold and hot end of the semiconductor (°C)

BTMS battery thermal management system

EV electric vehicle

HEV hybrid electric vehicle

ICE internal combustion engine

TEC thermoelectric cooling

SBTMS semiconductor-based BTMS

OCV open-circuit voltage

HPPC hybrid pulse power characterization

PRSM polynomial responding surface model

CFD computational fluid dynamics

FEM finite element method

ABTMS air-cooled BTMS